AIMS Materials Science, 4(5): 1095-1121.
DOI: 10.3934/matersci.2017.5.1095
Received: 06 September 2017
Accepted: 24 October 2017
Published: 30 October 2017

http://www.aimspress.com/journal/Materials

Research article

Optical and structural characterization of ZnSe thin film fabricated by thermal vapour deposition technique

Mohammed Tareque Chowdhury [1], Md. Abdullah Zubair [2,*], Hiroaki Takeda [3], Kazi Md. Amjad Hussain [1], and Md. Fakhrul Islam [2]

[1] Experimental Physics Division, Atomic Energy Centre, Bangladesh Atomic Energy Commission, Dhaka, Bangladesh
[2] Department of Glass and Ceramic Engineering, Bangladesh University of Engineering and Technology (BUET), Dhaka, Bangladesh
[3] School of Materials and Chemical Technology, Tokyo Institute of Technology, Tokyo, Japan

*** Correspondence:** Email: mazubair2017@gmail.com; Tel: +8801952753719.

Abstract: Zinc-selenide thin film was prepared on a soda-lime glass substrate by thermal vapor deposition technique. The X-ray diffraction data confirmed the cubic zincblende structure with a preferred orientation along (111) plane. Different models such as Debye-Scherrer, Size-Strain plot, Williamson-Hall, uniform stress deformation model and uniform deformation energy density model and the so called approximation model were adopted to analyse the XRD data. Detailed microstructural parameters such as crystallite size, strain, stress, isotropic energy density, dislocation denstiy were reported and discussed in comparison with scanning electron microscopy data. The transmission spectra was obtained by UV-Vis-NIR spectrometer in the range of 250–2500 nm at room temperature. Important optical constantssuch as refractive index and dielectric constant was estimated using Swanepoel's envelope method. The same method was used to check the thin film thickness which was found to be ~374.9 nm and this thickness was further confirmed by Scanning Electron Microscopy (368.3 ± 19.1 nm). The optical band gap was estimated to be 2.64 e*V*. The dispersion of refractive index was discussed interms of empirical Cauchy dispersion relation and the dispersion was further analysed by Wemple-DiDomenico Single oscillator model which provide physically meaningful parameters such as static refractive index, oscillator energy and dispersion energy. Both the structural and optical data not only complemented each other but also implied that good quality Zinc-selenide thin film could be deposited on ordinary glass substrates.

Keywords: Zinc-selenide; thin film; texture analysis; pole-figure; transmission spectra; interference fringes; optical band gap; optical constants

1. Introduction

Zinc-selenide (ZnSe) is a II-VI group direct band gap compound semiconductor which is one of the most famous mono-chalcogenides because of its superior optical and semiconducting properties. Due to large band gap and optical transparency in the visible and infrared region, ZnSe can be used as a window layer in thin film solar cells [1,2,3]. It can also be used for other optoelectronic devices such as, light emitting and laser diodes, luminescent devices etc. [4–7]. Many chemical and physical vapour processes are used for deposition of ZnSe thin films [8,9]. Sol-gel, spray pyrolysis, chemical bath deposition method involve complicated chemical reactions and at the same time chemical precursors have to be optimised to prepare single phase ZnSe thin film. In the chemical deposition process, the crystallinity and the surface morphology was not always suitable for optoelectronic and many memory devices. The main advantage of thermal vapour deposition in comparison with chemical process is that stoichiometry can be directly transferred from the source powder to the substrate by evaporating source material. Numerous articles were published in the recent years regarding the optical and structural characterization of thermal vapour deposited (TVD) ZnSe thin film on different types of substrates: Si (100), fused silica glass, borosilicate glass, indium-tin-oxide coated glass and soda-lime glass [6,10–20]. The vacuum pressure was also varied from a very large value (1 Pa for close space sublimation) to a very small value (3×10^{-5} Pa for PLD) depending on the selection of different deposition systems [6,10–18,20,21,22]. The evolution of structural and optical properties of the ZnSe thin films have been found to depend greatly on substrate specification and vacuum pressure as well as on the substrate temperature and post-deposition thermal treatment conditions. In a nutshell, a careful selection of process-parameters plays a pivotal role in attaining the desired properties of thin films. Thus research opportunities in this arena are yet to be explored.

Recently, Hassanien et al. reported an elaborate optical characterization with in-depth quantitative model analysis for pulsed laser annealed TVD ZnSe where crystallinity was found to improve significantly with increase in laser power from 10 to 30 W [6]. However, the major focus of their report was not concentrated towards the detailed crystallographic, geometrical, structural and microstructural parameter analysis in correlation with the optical response of the film. Similarly, Desai et al. discussed the details of the optical characteristics of a single TVD ZnSe film on glass substrate, where no structural data was presented in connection with the observed optical parameters [12]. Khan et al. also reported the annealing temperature dependent XRD data of the TVD ZnSe thin film on borosilicate glass. Although (111) peak intensity was found to increase with the annealing temperature from 350 to 500 ℃, no (220) or (311) peak was observed in any of the thin film [13]. Hence, it was rather difficult to make any conclusive remark on the structure property relation based on only a single peak. Absence of (220) and (311) peaks in ZnSe thin film was also reported elsewhere [21,22]. Similar type of structural data was also observed for TVD ZnSe thin film on soda-lime glass substrate by Gullu et al.. Faint peaks corresponding to (220) and (311) planes appeared in the diffraction pattern only for post-deposition annealing treatment at 500 ℃ [23]. However, temperature as high as 500 ℃ could have detrimental impacts on the thermo-mechanical and chemical properties of soda-lime glass. Post-deposition annealing of TVD ZnSe thin film on glass substrate by Ashraf et al. was reported to substantially enhance the intensity of the (111) peak with little effect on the existing (220) and (311) peaks at high angles with negligible intensities [20]. Inadequate vacuum pressure could be the possible reason for (220) and (311) peaks to be faint. Aqili et al. also reported similar XRD data for ZnSe thin film deposited by closed sublimation method [18].

Khairnar reported XRD data of TVD ZnSe on glass substrate where only (111) peak was observed [19]. No other structural data were reported in connection to the optical properties of the thin film. However, Zhang et al. reported excellent XRD patterns for pulsed laser deposited ZnSe thin film on fused quartz and GaAs substrates, where all three (111), (220) and (311) peaks were observed for pure ZnSe thin film [16]. In their report, phase transformation from zincblende to wurtzite structure with nitrogen-doping was rather elegantly elucidation by explicating the appearance of Raman peaks using the 1st principle calculations. However, Kalita et al. performed some detailed structural parameter analysis on TVD ZnSe thin films where substrate temperature was varied from 30 to 350 ℃ during deposition. There, the (220) and (311) peak-intensities appeared to increase rather noticeably above 300 ℃ substrate temperature. Recently, Mittal et al. deposited ZnSe thin film using thermal vapour deposition and magnetron sputtering techniques on Si, SiO_2-glass and Ge substrates, where the reported XRD pattern of the TVD ZnSe thin film on Si substrate shows the existence of all three peaks [10]. In their report, elaborate microstructural and surface-morphological analyses were done for the structural characterization and the major emphasis was put particularly on the wave-guide application of the ZnSe thin films. Generally XRD data of many nanoparticles, nanocomposites and thin films were used for structural characterization adopting not only the simple Debye equation but also the modified Debye relation, modified Williamson-Hall relation named as uniform stress density model (USDM), uniform deformation energy density model (UDEDM) and size-strain plot (SSP) [24–30]. In addition to that, Bushroa et al. used semi analytical function to extract size, strain data for TiSiN thin film deposited by magnetron sputtering technique [31]. However, reports are yet to be published for ZnSe thin film adopting all these aforementioned models.

Although in the recent years, a considerable amount of studies have been carried out either on the optical or structural properties of ZnSe thin films prepared under different conditions, a little emphasis has been given on both the optical and structural properties together, which is vital for film-quality assurance and device applications. Thus, there is an ample of room for conducting elaborate studies that tends to bridge the two aspects of the concerned thin film. Therefore, the primary objective of this paper is to study the TVD ZnSe thin film on a common soda-lime glass substrate through detailed structural analysis including crystallographic, geometrical and microstructural parameters using XRD, SEM and different deformation models. At the same time, various optical parameters have been analysed using the interference patterns present in the optical transmission spectra, so as to establish any meaningful correlation between the structural features and optical parameters of a single TVD ZnSe thin film on an ordinary substrate. The study will also acts as a catalyst to conduct further detailed research on the influence of process variables and chemical compositions on the properties chalcogenide based thin films.

2. Materials and Method

ZnSe thin film is prepared by thermal evaporation of ZnSe powder on a normal inexpensive soda-lime glass substrate which was at first, thoroughly cleaned ultrasonically in acetone bath for an hour followed by rinsing with de-ionized water numerous times. Then the substrate was left inside a vacuum desiccator filled with moisture absorbing fresh silica-gel for 24 hrs to dry. Coarse ZnSe aggregates were crushed into fine powder which was then directly put in a molybdenum boat inside the vacuum chamber of a thermal evaporator (model: EU300).The clean substrate was clamped

directly on top of the boat together with a custom-designed tin-mask to control the deposition area. The evaporation process was carried out at a vacuum pressure of approximately 10^{-4} Pa. The deposition rate was controlled by adjusting the Variac manually. During the deposition process, the substrate was kept at 300 ℃. The thickness and deposition rate were monitored by quartz crystal oscillator. The deposition rate was kept around 0.2 nm/sec. The deposited thin film was then annealed at an elevated substrate temperature of 350 ℃ for 1 hour under the same vacuum atmosphere in order to ensure that no oxidation of the film could take place and at the same time the source was allowed to cool down.

The crystal structure and the initial phase identification of the thin film was performed by PANalytical X-ray diffractometer (Model: EMPYREAN, PANalytical, Almelo, Netherland) adopting Bragg-Brentano geometry with parallel beam optics configuration. The diffractometer was operated at 45 kV and 40 mA and the experiment was carried out at room temperature. For crystallographic orientation analysis, a special diffractometer optical configuration required by the Schulz reflection method was adopted for the X-ray intensity-data collection and the commercial X'pert TEXTURE software (Version 1.2, PANalytical B.V., Almelo, Netherlands) supplied by PANalytical was utilized to construct 3D pole-figures. thin film surface morphology and cross-section were observed by Field Emmission Sanning Electron Microscope (FESEM) (model: JSM 7600F, JEOL, JAPAN). Transmission spectra of both ZnSe film deposited glass substrate and clean substrate without the film were collected within a wavelength range of 250–2500 nm with respect to air at room temperature using a dual beam UV-Vis-NIR spectrophotometer (model: LAMBDA 1050, Perkin-Elmer, USA) equipped with three detector module. The diffuse reflectance spectra of ZnSe source powder was also collected at room temperature by replacing the three detector module with 150 mm integrating sphere, where spectralon standard supplied by Perkin-Elmer was used as a reference sample.

3. Results and Discussion

3.1. Structural Characterization

Figure 1(a) shows the X-ray diffraction (XRD) spectra of ZnSe thin film. The most intense peak was identified for (111) plane at $2\theta = 27.20°$ and the crystal strcuture was nicely matched with cubic zincblende structure (ICDD 01-071-5978). The other two peaks were observed at $2\theta = 45.23°$ and $53.15°$ correspond to (220) and (311) planes repectively. Although a similar preffered orientation had also been observed in a previous report [6] the observed relative intensity of (311) peak with respect to (220) peak appear to be different. At the same time, in Figure 1, the (311) to (220) peak intensity ratio appears to be greater and smaller than one for the film and the source powder respectively. Such anomalies have been dealt-with through thin film texture analysis at the end of this section. Moreover, in contrast to our observation, the existence of purely hexagonal wurtzite structure or a mixture of cubic zincblende and hexagonal wurtzite structures were also reported for ZnSe thin films deposited by different methods indicating the influence of deposition technique on phase formation [13,16]. The absence of any peak other than those for ZnSe in the diffraction pattern of our thin film suggests that the applied vacuum during the deposition process was good enough to prevent the formation of any stable oxide like ZnO as reported to form earlier [32].

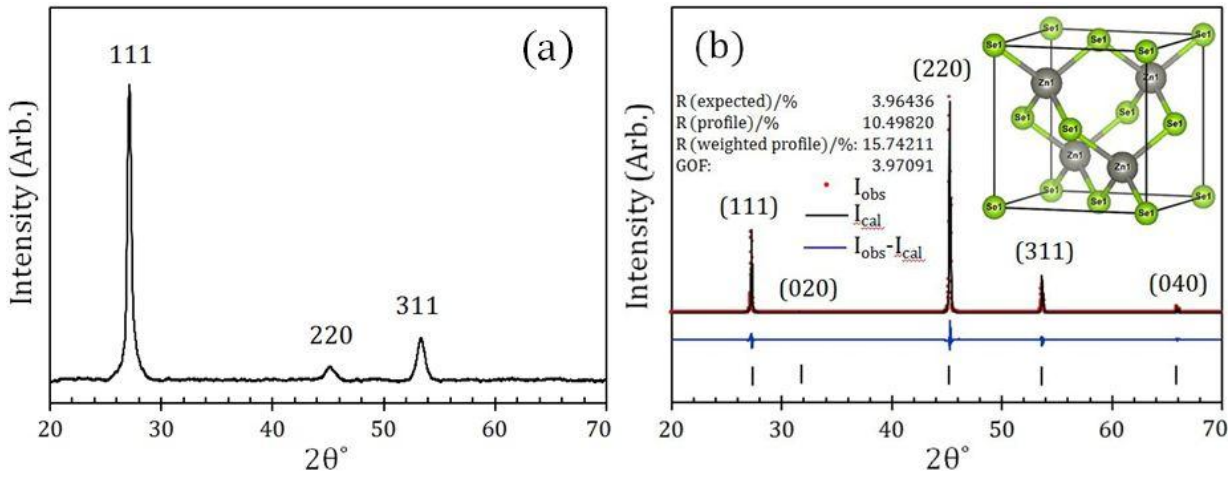

Figure 1. (a) X-ray diffraction spectra of ZnSe thin film; (b) Powder XRD pattern for ZnSe corresponds to red dot, black solid line refers to calculated (Rietveld fitting) and sky-blue solid line refers to the difference between observed and Rietveld fitting data.

However, it is worth mentioning that in a previous report by M. Ashraf et al. [20] where ZnSe thin films were thermally deposited on soda-lime glass substrate with 25 ℃ substrate temperature, (111) peak intensity gradually increased with increasing post-annealing temperature from 100 to 300 ℃, which was attributed a gradual increase in crystallinity of the thin films. In contrast to that, (220) and (311) peak intensities remained either quite low or nonexistent [13] irrespective of post annealing temperature. However, the XRD pattern of pulse laser deposited ZnSe thin film on fused quartz substrate at 400 ℃ reported by Zhang et al. [16] exactly matches the peak intensity pattern as observed in our case (Figure 1(a)), where the (111), (311) and (220) peak-intensities can be found to change in a descending order. Additionally, the relative intensities of all the three peaks in both of our studies appear to be rather noticeable. This observation is in fact rather promising in a sense that it allowed us to perform crystallographic orientation analysis of the film with respect to all three planes observed (as shown at the end of this section), which has not yet been reported in any scientific literature for the TVD ZnSe films to the best of our knowledge.

Figure 1(b) shows Rietveld analysis results obtained from X'Pert HighScore Plus (Version 4.1, PANalytical B.V., Almelo, Netherlands) software for ZnSe source powder, with various fitting parameters listed in the upper left corner of the figure. Both goodness of fit (GOF) and R-factors appear to fall within acceptable range. The source powder has been found to have cubic symmetry with F-43m space group. Since Rietveld refinement method cannot be used to estimate the lattice parameters from thin film XRD data due to poor signal to noise ratio, an alternative approach was adopted to estimate the lattice parameter known as Nelson-Riley relation given in the equation below [33]:

$$f(\theta) = \frac{1}{2}\left[\frac{cos^2\theta}{sin\theta} + \frac{cos^2\theta}{\theta}\right] \quad (1)$$

Figure 2 shows the lattice parameter "a" as a function of Nelson-Riley error function $f(\theta)$, where "a" is given by the following equation for cubic system:

$$a = \frac{\lambda\sqrt{h^2+k^2+l^2}}{2sin\theta} \quad (2)$$

The least square fitted line equation is given at the bottom right corner of the figure. The accurate lattice parameter of the thin film corresponds to the value of y at which $x(= f(\theta)) = 0$. A similar approach was adopted to calculate the ZnSe thin film lattice parameter by Kalita et al. [4]. The corrected lattice parameter estimated from Figure 2 is, a = 5.683 Å shows good agreement with previously reported result [4].

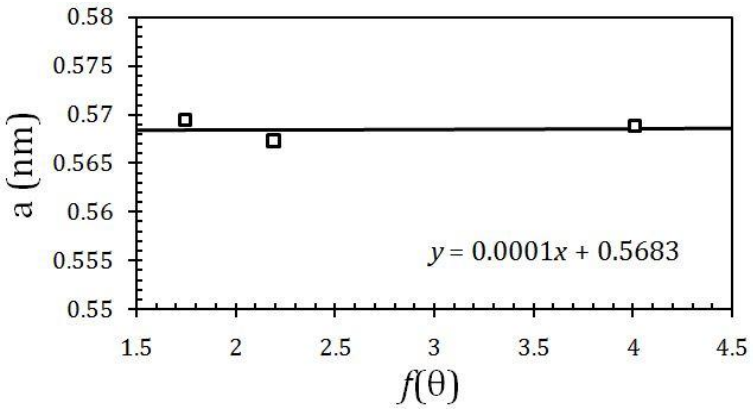

Figure 2. Nelson-Riley error function ($f(\theta)$) relation to estmate the lattice parameter of ZnSe thin film.

Lattice parameter of ZnSe powder estimated using Rietveld refinement method exhibites smaller value than what we have obtained from Nelson-Riley relation. The powder diffraction pattern and the corresponding Rietveld refinement are shown in Figure 1(b) along with the ZnSe unit cell in inset. The structural parameters obtained from Rietveld refinement confirms F-43m space group with cubic zincblende symmetry for ZnSe powder, where the Se atoms reside in all the face centered cubic positions and the Zn atoms occupy one-half of the tetrahedral sites in an alternating manner axially. The lattice parameters for powder and thin film are given in Table 1 below.

Table 1. Lalttice parameters ZnSe source powder and thin film.

Lattice constant	Rietveld refinement (source powder)	Nelson-Riley method (ZnSe thin film)	Lattice volume strain
a (Å)	5.663	5.683	0.0106

Thus it is also possible to estimate the lattice volume strain given in the 4th column of Table 1 using the following equation:

$$\frac{\Delta V}{V} = \frac{(a+\Delta a)(b+\Delta b)(c+\Delta c)-abc}{abc} \quad (3)$$

where, a, b and c are the dimensions of the unit cell and Δa, Δb and Δc are the changes in lattice dimensions. Now, equation (3) can be written as:

$$\frac{\Delta V}{V} = (1+\varepsilon_1)(1+\varepsilon_2)(1+\varepsilon_3) - 1 \tag{4}$$

where, $\varepsilon_1 = \Delta a/a$, $\varepsilon_2 = \Delta b/b$, $\varepsilon_3 = \Delta c/c$. When, $\varepsilon_{1,2,3} \ll 1$, then equation (4) can be approximated as:

$$\frac{\Delta V}{V} \approx \varepsilon_1 + \varepsilon_2 + \varepsilon_3 \tag{5}$$

Assuming isotropic strain in the cubic lattice we get: $\varepsilon_1 = \varepsilon_2 = \varepsilon_3 = \varepsilon$. Hence, equation (5) can be simplified to:

$$\frac{\Delta V}{V} \approx 3\varepsilon \tag{6}$$

where, $\varepsilon = \frac{a_{thinfilm} - a_{sourcepowder}}{a_{sourcepowder}}$.

The XRD data can also be used to estimate the crystallite size and the average strain generated in the thin film. XRD profile is a convolution of instrumental line broadening and physical or structural broadening. The structural line broadening is in turn is associated with size broadening and strain broadening.

Now, assuming Lorentzian XRD line profile we can write,

$$\beta_T = \beta_{struct.} + \beta_{inst.} \tag{7}$$

$$\beta_{struct.} = \beta_{cryst.} + \beta_{str.} \tag{8}$$

$$\beta_T = \beta_{cryst.} + \beta_{str.} + \beta_{inst.} \tag{9}$$

where, β_T, $\beta_{struct.}$, $\beta_{cryst.}$, $\beta_{str.}$ and $\beta_{inst.}$ are spectral width (FWHM) of the observed peak, structural line broadening, size broadening, strain broadening, and instrumental line broadening respectively. Here, $\beta_{inst.}$ is obtained from NIST (National Institute of Science and Tech) standard sample: Lanthanum hexaboride (LaB_6). Therefore, $\beta_{struct.}$ can be extracted from β_T using equation (7). The most well-known relation between crystalline size and line broadening is the Debye-Scherrer relation which is given by (12):

$$\beta = \frac{k\lambda}{D cos\theta} = \frac{k\lambda}{D}\frac{1}{cos\theta} \tag{10}$$

where, *D* is the crystallite size, β is equivalent to FWHM for structural broadening ($\beta_{struct.}$) obtained from equation (7) for low index and high intensity peak, k is approximated as 0.9 and λ = 1.54 Å is X-ray wavelength. Therefore, *D* estimated from (111) peak in Figure 1(a) in the present case comes out to be 13.3 nm.

In principle, the crystallite size should be independent of $\beta cos\theta$ in the equation (10). However, experimentally $\beta cos\theta$ can be found to vary as 0.010, 0.013, 0.012 for (111), (220) and (311) planes, respectively. It means that for each reflection plane, the crystallite size varies according to equation (10), which cannot be true. Therefore, an error is introduced in the crystallite size estimation. To minimise the error, equation (10) can be modified as follows [28]:

$$\ln\beta = \ln\frac{k\lambda}{D} + \ln\frac{1}{cos\theta} \tag{11}$$

A plot of $\ln\beta$ against $\ln(1/cos\theta)$ along with the corresponding least square fitted equation is depicted in Figure 3(a). In principle, if there is no systematic error that is, if equation (10) holds for experimental data, the slope of the fitted line should be 1. However, in case of present experimental data the slope has been found to be greater than 1 (~3.4) due to a more pronounced θ dependence of $\beta cos\theta$ than that required for maintaining a fixed *D* value.

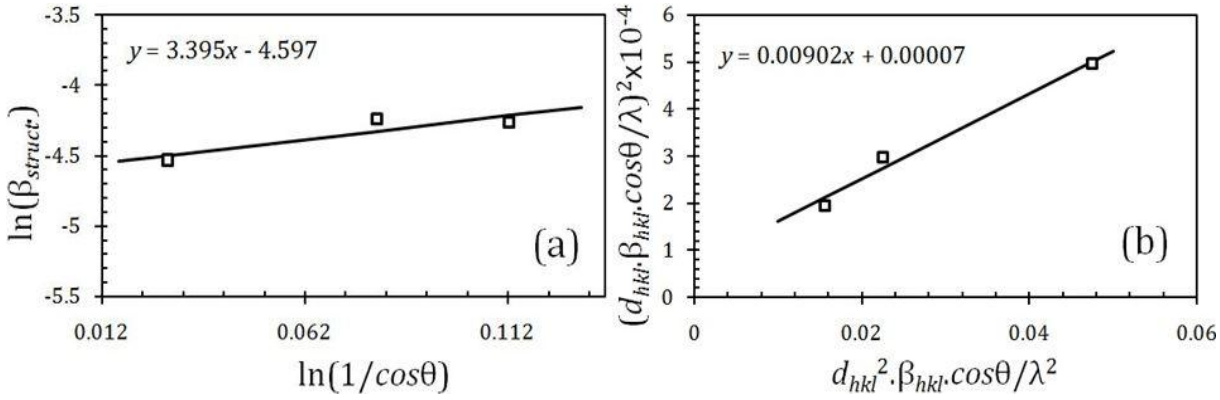

Figure 3. (a) Modified Debye-Scherrer model, (b) SSP method, along with the corresponding equations required for linear fit.

Now following equation (11), at $\ln(1/\cos\theta) = 0$, the Y-axis intercept can be related to the size of the crystallite as follows:

$$\ln\beta = \ln\frac{k\lambda}{D} = -4.597$$

$$\text{or, } D = \frac{k\lambda}{e^{\ln\beta}} \tag{12}$$

The crystallite size estimated from equation (12) is 13.7 nm. However, lattice strain cannot be calculated from the modified Debye-Scherrer relation. The size and strain have been estimated using Size-strain plot (SSP). In this estimation, the peak profiles due to strain were assumed to be Gaussian and crystallite size as Lorentzian. The SSP relation is expressed as [30]:

$$(d_{hkl}\beta_{hkl}cos\theta/\lambda)^2 = \frac{k}{D}(d_{hkl}^2\beta_{hkl}cos\theta/\lambda^2) + \left(\frac{\varepsilon}{2}\right)^2 \tag{13}$$

where, d_{hkl} is the interplanner spacing calculated using the standard Bragg's law, β_{hkl} is the FWHM for structural broadening, k is approximated to 3/4 for spherical shape, ε is the average strain, θ is the Bragg angle and *D* is the crystal size. The standard plot for SSP model is shown in the Figure 3(b). Here, the crystallite size has been estimated as 12.8 nm and the strain in the film has been determined to be 1.70×10^{-2} from the slope and Y-intercept of the least square fitted solid line given by the equation at the top left corner of the figure, respectively.

The size and strain have further been estimated adopting the basic Williamson-Hall (W-H) relation [15], which can be directly derived by combining the basic Scherrer formula (equation (10), where, $\beta = \beta_{cryst.}$), the equation for strain broadening given by: $\beta_{srt.} = 4\varepsilon \cdot \tan\theta$ and the relation for structural broadening (equation (8)) as below:

$$\beta_{struct.} = \beta_{cryst.} + \beta_{str.} = \frac{k\lambda}{Dcos\theta} + 4\varepsilon \cdot \tan\theta \tag{14}$$

The above equation can simply be rearranged as:

$$\beta_{hkl}cos\theta = \frac{k\lambda}{D} + 4\varepsilon\, sin\theta \tag{15}$$

Here, $\beta_{hkl}(\equiv \beta_{struct.})$ is the FWHM for structural broadening, D is the size of the crystal, ε is the strain, λ is the X-ray wavelength and k is a constant approximated to 0.9. This equation is also known as the uniform deformation model (UDM) and it is assumed that the strain is uniform in all crystallographic directions.

Figure 4(a) depicts the plot of $\beta_{hkl}cos\theta$ vs. $4sin\theta$ along with the least square fitted linear equation in the inset. The slope of the fitted equation corresponds to strain and the Y-intercept corresponds to the size of the crystallite as λ and k are already known. The basic W-H relation (UDM) can be modified using the Hooke's law with the assumption of uniform stress (σ) and the anisotropic strain ε_{hkl} as follows:

$$\varepsilon_{hkl} = \frac{\sigma}{E_{hkl}} \tag{16}$$

The modified model is known as the uniform stress deformation model (USDM). The analytical function for the USDM can be expressed by replacing ε with ε_{hkl} in equation (15) and then equating with equation (16) as follows:

$$\beta_{hkl}cos\theta = \frac{k\lambda}{D} + 4\varepsilon_{hkl}\, sin\theta = \frac{k\lambda}{D} + 4\frac{\sigma}{E_{hkl}}\, sin\theta \tag{17}$$

However, for cubic systems, the elastic modulus E_{hkl} is related to elastic compliance S_{11}, S_{12}, S_{44} and *hkl* index of the corresponding plane by the following relation:

$$\frac{1}{E_{hkl}} = \frac{S_{11} - 2(S_{11} - S_{12} - S_{44})\left(h^2k^2 + k^2l^2 + l^2h^2\right)}{\left(h^2 + k^2 + l^2\right)^2} \tag{18}$$

Here, the elastic compliances are calculated from elastic stiffness (C_{mn}) values using the following relations:

$$S_{11} = \frac{C_{11} + C_{12}}{(C_{11} - C_{12})(C_{11} + 2C_{12})};\ S_{12} = \frac{-C_{12}}{(C_{11} - C_{12})(C_{11} + 2C_{12})};\ S_{44} = \frac{1}{C_{44}} \tag{19}$$

where C_{11}, C_{12} and C_{14} are 80.7, 48.8 and 44.1 GPa, respectively. In Figure 4(b), $\beta_{hkl}cos\theta$ is plotted against $(4/E_{hkl})\, sin\theta$. The slope of the plot after least square fitting the data with linear equation given in the inset corresponds to the stress, which is 103.17 MPa and the Y-intercept of the fitted line is related to the size of the crystal which is estimated as 13.7 nm. The W-H relation can be further

modified to calculate the isotropic deformation energy density of a crystal by assuming both the stress and strain to be anisotropic according to:

$$u = \frac{1}{2}\varepsilon_{hkl}\sigma_{hkl} = \left(\frac{{\varepsilon_{hkl}}^2 E_{hkl}}{2}\right) \tag{20}$$

This model is known as uniform deformation energy density model (UDEDM) and can be expressed by combining equations (17) and (20) as:

$$\beta_{hkl}cos\theta = \frac{k\lambda}{D} + 4\varepsilon_{hkl}\, sin\theta = \frac{k\lambda}{D} + 4\left(\frac{2u}{E_{hkl}}\right)^{\frac{1}{2}} sin\theta \tag{21}$$

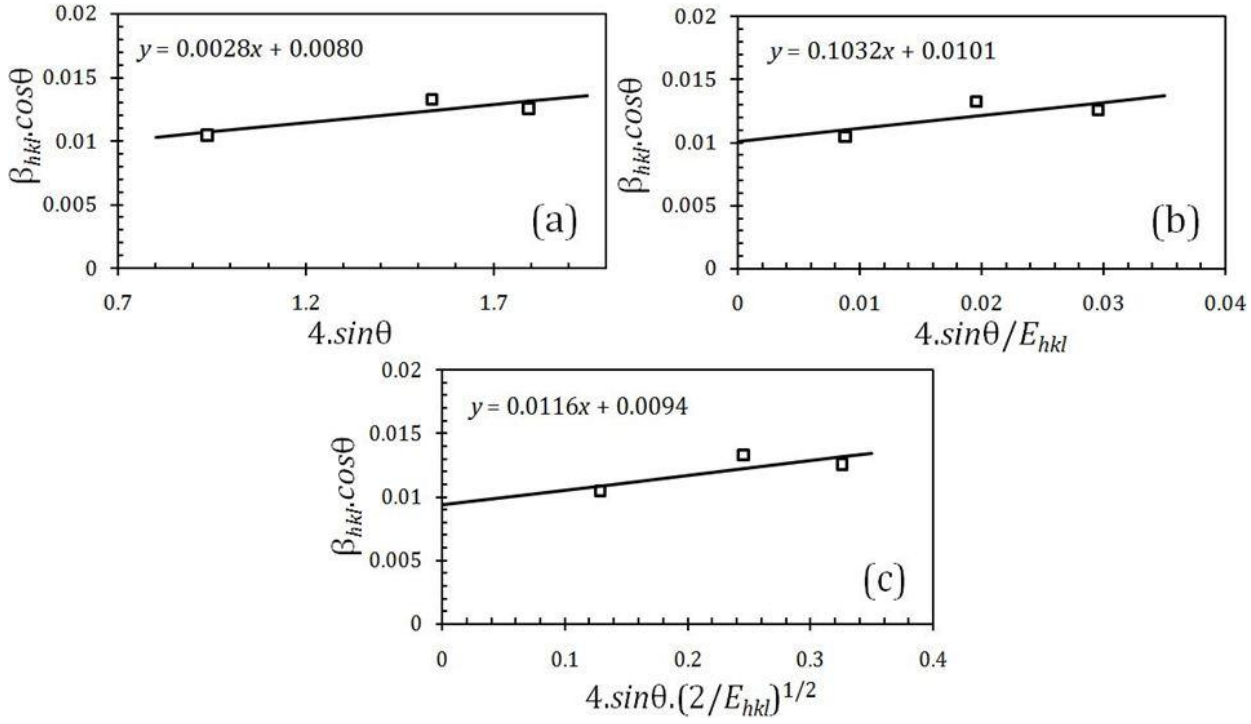

Figure 4. (a) Basic W-H model: UDM, (b) modified W-H model: USDM, (c) modified W-H model: UDEDM for ZnSe thin film along with correspond equations required for the linear fits.

In Figure 4(c), $\beta_{hkl}cos\theta$ is plotted as a function of $4(2u/E_{hkl})^{\frac{1}{2}} \cdot sin\theta$. The slope of the line after least square fitting the data, represented by the linear equation in the inset determines the deformation energy density of the crystal and it is estimated as 134.53 kJ/m^3. The size of the crystallite has been estimated as 14.8 nm from the Y-intercept of the fitted line. The dislocation density has also been calculated using the relation:

$$\rho = \frac{1}{D^2} \tag{22}$$

However, according to a recently proposed approximation method [31], the experimental XRD peak profile width is a convolution of size and strain broadening. Here the size and strain broadening profile was approximated using two analytical functions $M(x)$ and $N(x)$, given by [31]:

$$M(x) = (1 + \gamma x^2)^{-1} \tag{23}$$

$$N(x) = (1 + \gamma x^2)^{-2} \tag{24}$$

where γ is a constant coefficient.

Here, the structural broadening was calculated by subtracting the instrumental broadening from the total broadening at different Bragg angles. For structural characterization two peaks were selected: (111) and (311) at 2θ = 27.13 ° and 53.32 ° respectively. For these two observed peaks the experimental structural line broadening β_1 and β_2 were estimated in terms of FWHM. Now following some manipulations of equations (23) and (24) it was shown [31]:

$$\frac{m_1}{\beta_1} = \frac{1}{2}\left[1 - 4\frac{n_1}{\beta_1} + \sqrt{1 + 8\left(\frac{n_1}{\beta_1}\right)}\right] \tag{25}$$

$$\frac{\beta_2}{\beta_1} = \frac{\left\{\left[V\left(\frac{m_1}{\beta_1}\right)\right] + \left[2\left(\frac{n_1}{\beta_1}\right)W\right]\right\}^2}{\left[V\left(\frac{m_1}{\beta_1}\right)\right] + \left[4\left(\frac{n_1}{\beta_1}\right)W\right]} \tag{26}$$

$$\frac{n_2}{\beta_2} = \frac{n_1}{\beta_1} \times \frac{W}{\beta_2/\beta_1} \tag{27}$$

where, m_1 and m_2 are the size broadening contributions to (111) and (311) peaks respectively and n_1 and n_2 are the strain broadening contributions to (111) and (311) peaks, respectively.

Here, V and W are expressed as [31]:

$$V = \frac{m_2}{m_1} = \frac{Cos\theta_{111}}{Cos\theta_{311}} \tag{28}$$

$$W = \frac{n_2}{n_1} = \frac{tan\theta_{311}}{tan\theta_{111}} \tag{29}$$

Now, Figure 5 shows m_1/β_1 as a function of β_2/β_1 calculated using equations (25) and (26). From this plot experimental m_1/β_1 can be extracted from the corresponding experimental β_2/β_1 ratio as shown by the dotted line intersecting the left-hand-side vertical axis. Since m_1 is the size broadening contribution to experimental β_1, the crystal size could be calculated using Scherrer formula given as:

$$D = \frac{k\lambda}{m_1 cos\theta_{111}} \tag{30}$$

Here, m_1 = (experimental m_1/β_1 ratio) × β_1 , D is the size of the crystal, k is a constant equal to 0.9, λ is the wavelength of the X-ray radiation and θ_{111} is the Bragg angle for (111) peak. Following equation (30), the crystal size can found to be 15.4 nm.

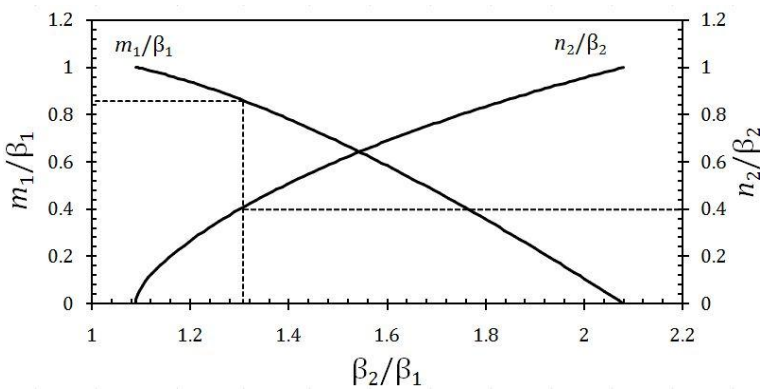

Figure 5. m_1/β_1 and $n_2/\beta_1$was plotted as a function of β_2/β_1.

Figure 5 also shows n_2/β_2 as a function of β_2/β_1 calculated using equations (26) and (27), where, the experimental n_2/β_2 can also be extracted from the corresponding experimental β_2/β_1 ratio as shown by the dotted line intersecting the right-hand-side vertical axis. Since n_2 is the strain broadening contribution to experimental β_2, the strain could be calculated using the following formula given as:

$$\varepsilon = \frac{n_2}{4tan\theta_{311}} \tag{31}$$

Here, n_2 = (experimental n_2/β_2 ratio) $\times$ β_2, ε is the strain and θ_{311} is the Bragg angle for (311) peak. Following equation (31), the strain has been estimated to be 5.90 $\times 10^{-3}$. Figure 6(a) shows scanning electron microscopic (SEM) image of the ZnSe thin film surface and the corresponding particle size distribution determined from several such micrographs using the ImageJ software (Version 1.46r) is also given in Figure 6(b).

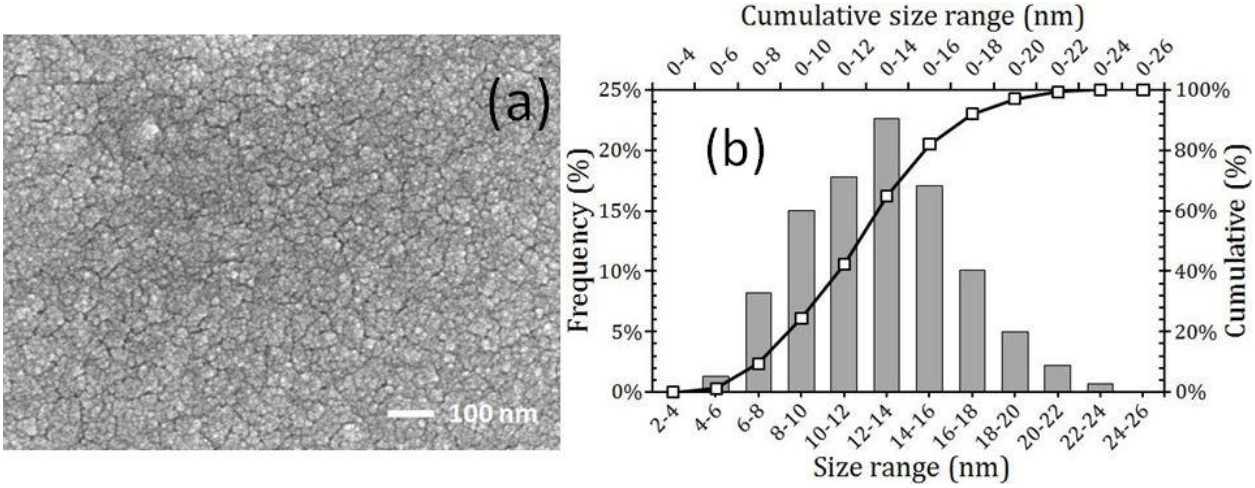

Figure 6. (a) ZnSe thin film SEM micrograph with 100 nm scale bar, (b) particle size distribution estimated from the SEM micrograph.

The most probable particle size can be found to be around 12–14 nm from the size distribution histogram. Table 2 shows the detailed structural and geometrical parameters obtained from the XRD data analysis using different models and SEM.

Table 2. List of microstructural and geometrical parameters.

Method	D (nm)	ε	σ (MPa)	u (kJ m^{-3})	ρ (nm^{-2})	R^2
Debye-Scherrer	13.3				5.68×10^{-3}	
Modified Debye-Scherrer	13.7				5.29×10^{-3}	0.80
SSP	12.8	1.70×10^{-2}			6.09×10^{-3}	0.98
UDM	17.2	2.84×10^{-3}			3.36×10^{-3}	0.73
USDM	13.7	*1.33×10^{-3}	103.17		5.29×10^{-3}	0.54
UDEDM	14.8	*1.85×10^{-3}	*147.29	134.53	4.57×10^{-3}	0.62
Approximation technique	15.4	5.90×10^{-3}			4.18×10^{-3}	
SEM	12–14				$(5.1–6.22) \times 10^{-3}$	

* Average value calculated from three different crystallographic directions: (111), (220) and (311).

It is worth mentioning that a step-size of 0.05 ° has been used for the thin film XRD line scanning which is less than 1/10 of the observed FWHM (β_T) of the sharpest peak in Figure 1(a). This configuration gives us more than 10 data points for determining β_T with reasonable accuracy. In addition to that, the correlation coefficients (R^2) for least square fitting the structural broadening data with different models (Figures 3(a), 3(b) and 4(a–c)) appear to fall within the range 0.60–0.98, which is quite reasonable when compared with previously published data for CsI thin film [27].

It can be found that the results obtained from the XRD analysis show reasonable agreement with SEM. From the SEM image analysis (Figures 6) a range of particle size varying from 2 to 26 nm has been observed. It can also be found that around 80% of the particles have size within the range of 10 to 18 nm (Figure 6(b)) which is quite agreeable as far as the XRD data is concerned where the average crystal size has been found to fluctuate within a narrow range of 12 to 17 nm depending on the models adopted for size calculation. However, any marked difference between crystal/particle size range measured by XRD and micrographic analysis could be associated with formation of defects in a certain manner that gives rise to different crystallographic orientations in individual particles. This is particularly true in case the particle size obtained from electron microscopy is reasonably larger than the crystal size of the same sample obtained from XRD peak broadening effect since; the X-ray diffraction peaks under Bragg-Brentano configuration arise from coherently scattering domains with congruent orientations, parallel to the diffraction plane. When individual particles form by agglomeration of such coherent domains separated by interfaces either with sharp orientation contrast ideally represented by grain boundaries or small orientation mismatch (low angle interface) typically represented by a 2D region consisting of regularly spaced dislocations, the crystal size from XRD always comes out to be smaller than the particle size from micrograph. Although with SEM the high-angle boundaries are sometimes easily identifiable from surface morphology it is rather unlikely to locate any low angle interface. Hence, as in case of the present thin film sample the particle size range agrees with crystal size range, it can be assumed that the

individual particles in the SEM image are in general coherent in terms of crystallographic orientation. Therefore the dislocation densities calculated from equation (22) as tabulated in the 3rd column of Table 2 represents the dislocation population along the high angle grain boundaries with some dislocations distributed possibly in a random manner within the coherent crystals without forming any low angle interface.

The SEM micrograph in Figure 6(a) further reveals the existence of numerous micro-cracks brunching throughout film surface. Such formations could be associated with strain relaxation phenomenon. From the lattice parameter data listed in Table 1, it can be found that lattice parameter of the thin film is slightly larger than that of the strain-free source powder by 0.023 Å. This corresponds to a lattice volume strain of 1.06×10^{-2} in the thin film as estimated using equation (6). This volume-change of the unit cell of the crystal can be attributed to the local lattice strain. On the other hand the average thin film strain has been estimated as 1.70×10^{-2}, 5.90×10^{-3}, 2.84×10^{-3}, 1.33×10^{-3} and 1.85×10^{-3} using SSP, Approximation method, UDM, USDM and UDEDM respectively. Except for average internal strain estimated from SSP, the average internal strain values obtained from the other models are at least 47% less than the local lattice volume strain. This implies that the thin film could become relaxed by reducing its strain through formation of surface micro-cracks during cooling after deposition. Therefore, under the above circumstances, it can be presumed that the average film strains obtained from either the basic and modified W-H models or the approximation method are more self-explanatory compared to that obtained from SSP method in our case. However, a more detailed study is required to reach to any definite or decisive conclusion on the above issue, which is underway. Nevertheless, it can safely be said that estimated crystallite size, strain and dislocation density show good agreement with previously reported data [4].

For further crystallographic characterization, it is important to find out the orientation distribution of the diffracting planes/crystallites with respect to substrate-normal. The orientation distribution of any particular crystallographic plane can be determined by constructing pole-figure, which is regarded as an essential visual tool for examining the texture of crystalline samples. In case of thin films, pole-figure is also used to check the quality of the surface in terms of the preferred crystallite orientation. For collecting the diffracted beam intensity data corresponding to a certain plane, the film was subjected to an in-plane rotation (represented by Φ-angle) from 0 to 360 ° at 3 ° interval at any given sample-surface tilt (represented by χ-angle) and the χ-angle was varied from 0 to 75 ° at same interval as Φ-angle. Then the intensity profile was further modelled up to a χ-angle of 90 ° to construct complete 3D pole-figures and the standard commercial X'pert TEXTURE software was used for that purpose. Three planes: (111), (220) and (311) were originally identified (Figure 1(a)) in the TVD ZnSe thin film XRD pattern under Bragg-Brentano configuration represented by 0 ° χ-angle and pole-figures corresponding to all three crystallographic planes were constructed as shown in Figure 7. The spherically anisotropic shape of the 3D pole-figures clearly indicates the existence of some sort of texture in our thin film sample. From the (111) pole-figure, it can be found that a major share of (111) plane is oriented at around 15 ° and 60 ° angles with the substrate plane normal. Contrary to that, the most intense peak has been observed for (111) plane in Figure 1(a). Such apparent discrepancy can be explained by the fact that even though the intensity count of (111) pole-figure at $\chi = 0$ ° is lower than that at $\chi = 15$ ° or 60 ° irrespective of Φ-angle it's absolute value is rather high compared to its (220) and (311) counterparts at 0 ° χ-angle, at least numerically. In addition to that, by comparing the XRD patterns of the ZnSe thin film (Figure 1(a)) and the source powder (Figure 1(b)), it can also be found that the (311) peak intensity in the film is quite significant

relative to that of the (220) peak, whereas the trend is exactly the opposite in the source powder. Such anomalous variation in relative peak intensity could be attributed to a distinctively sharp rise in intensity count observed in (311) pole-figure compared to that in (220) pole-figure around 0 °χ-angle representing the Bragg-Brentano geometrical configuration used for collecting the XRD patterns in Figure 1.

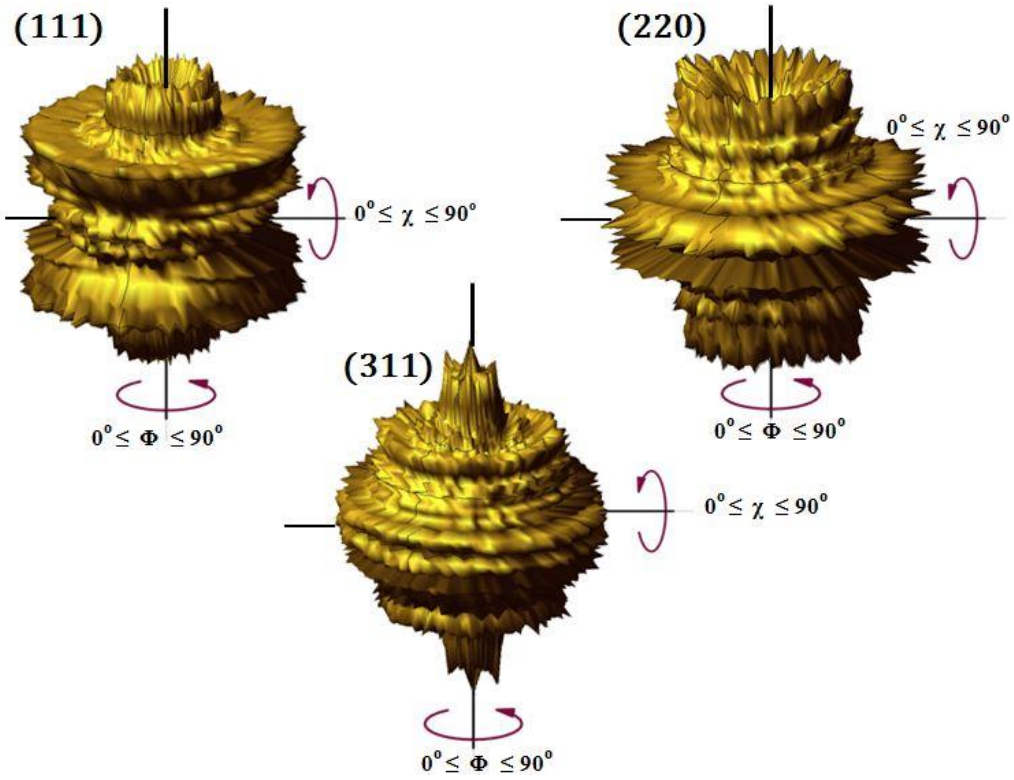

Figure7. Three dimensional pole-figure of ZnSe thin film.

However, to our knowledge, this is for the first time to report the orientation distributions of the three different planes so far. Previously, different groups have published pole-figure data for ZnSe thin films [34,35,36] but only for (111) plane, since it exhibited the most intense and legible peak under Bragg-Brentano configuration, which is consistent with our XRD data as well.

3.2. Optical Properties of ZnSe Thin Film

Figure 8(a) shows the transmittance spectra of ZnSe thin film. Two regions are found in the transmittance spectra. Region-I extending from 600 to 2500 nm, corresponds to transparent region since the incident wave passes through the thin film sample without being absorbed. The energy of the photon corresponding to these wavelengths is smaller than the band gap energy of ZnSe thin film. In this region a wavy nature in the spectra is observed. This is called the interference fringe or FECO (Fringes of Equally Chromatic Order). These interference pattern-like fringes are produced due to back and forth bouncing of the incident wave between three interfaces: film–air, film–substrate and substrate–air. In Region-II below 600 nm the transmittance drops sharply due to absorption of incident photon. The optical band gap can be estimated from this region.

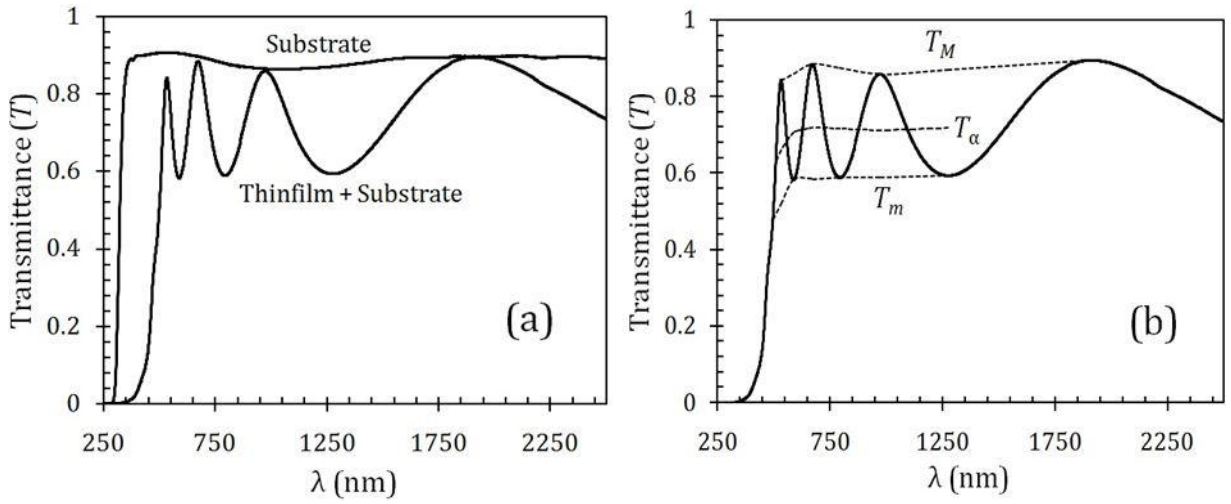

Figure 8. (a) Transmittance of ZnSe thin film deposited on soda-lime glass substrate, (b) Swanepoel's envelopes T_M and T_m; T_α refers to the geometric mean of T_M and T_m.

Figure 8(b) shows the three envelopes T_M, T_m and T_α in the transmittance spectra where $T_\alpha = \sqrt{T_M \cdot T_m}$. Since the FECO fringes give maxima and minima in transmittance spectra, the T_M and T_m corresponding to the top and bottom envelopes are obtained by interpolating the interference maxima and minima of the FECO fringes respectively using spline interpolation technique. Using Swanepoel's envelope method (SWEM), the refractive index of the thin film was estimated [37]. The refractive index has been calculated using the following equation [38]:

$$n_1^2 = \left[N(\lambda) + \{N(\lambda)^2 - S(\lambda)^2\}^{\frac{1}{2}}\right] \tag{32}$$

where, n_1 is the 1st approximation of the thin film refractive index and the parameter $N(\lambda)$ is expressed as follows;

$$N(\lambda) = 2S(\lambda) \cdot \left(\frac{T_M - T_m}{T_M T_m}\right) + \left\{\frac{S(\lambda)^2 + 1}{2}\right\} \tag{33}$$

where, $S(\lambda)$ is the substrate refractive index and can be expressed as:

$$S(\lambda) = \frac{1}{T_S} + \left(\frac{1}{T_S^2} - 1\right)^{\frac{1}{2}} \tag{34}$$

Here, T_S is the substrate transmittance which is a function of wavelength as shown in Figure 8(a). Knowing the n_1 value, a rough estimation of the thin film thickness (d_1) has been obtained using the following equation:

$$d_1 = \frac{\lambda_1 \lambda_2}{2\left[n_1(\lambda_2).\lambda_1 - n_1(\lambda_1).\lambda_2\right]} \tag{35}$$

where, λ_1 and λ_2 are the two wavelengths corresponding to two adjacent maxima (or minima) and $n_1(\lambda_1)$ and $n_1(\lambda_2)$ are the two corresponding refractive index values estimated from equations (32–34). Using the average value of d_1 and calculated n_1 it is possible to calculate the FECO order number m_o from basic interference equation given below:

$$2nd = m_o\lambda \tag{36}$$

T_M, T_m, n_1, d_1 and m_o at corresponding wavelength are listed in Table 3. Here, the thickness d_1 estimated using equation (35) shows strong wavelength dependence. The average d_1 is estimated to be 428.16 ± 56.17 nm. However, this fluctuation in thickness value can greatly be reduced by amending the calculated FECO order m_o values to the nearest exact integer for interference maxima and half integer for interference minima and then by using the revised FECO order *M* along with n_1 values in equation (36). The refined thickness values are now represented as d_2. Finally, a set of more refined refractive index (n_2) has been obtained by using corrected FECO order *M* and the average refined thickness in equation (36). The values of *M*, d_2 and n_2 are listed in Table 3. The average refined thickness ($d_{2(avg)}$) of the thin film is estimated as 374.94 ± 16.47 nm. Nonetheless, the film thickness measured from cross-sectional SEM image shown in Figure 9 can be found to be 368.26 ± 19.12 nm which is in good agreement with the thickness value obtained by optical method.

Table 3. Optical constants of ZnSe thin film using SWEM model.

λ	T_S	T_M	T_m	n_1	d_1	$d_{1(avg)}$	m_0	*M*	d_2	$d_{2(avg)}$	n_2
496	0.90		0.47								
532	0.90	0.84	0.51	2.78			4.49	4	381.43		2.83
588	0.90	0.85	0.58	2.56	379.27		3.74	3.5	400.39		2.74
672	0.89	0.88	0.58	2.63	504.35	428.16	3.36	3	382.16	374.94	2.68
793	0.87	0.87	0.58	2.67	435.72		2.89	2.5	369.89		2.64
972	0.86	0.85	0.58	2.69	393.31		2.37	2	360.03		2.59
1275	0.86	0.87	0.59	2.68			1.80	1.5	355.77		2.55
1912	0.89	0.89									

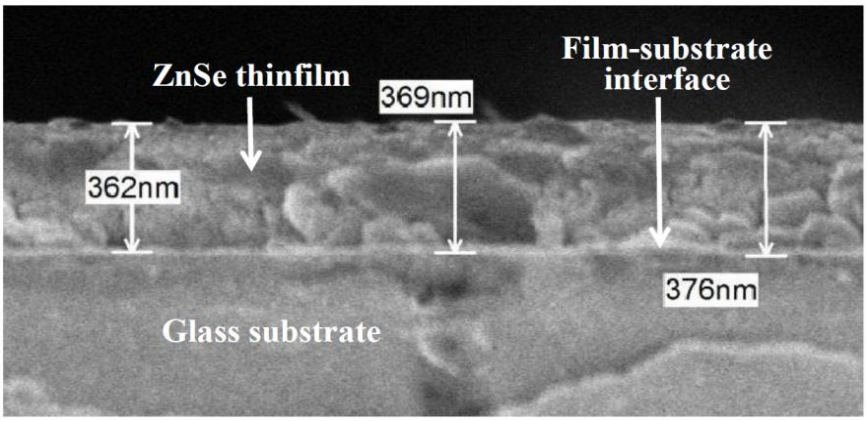

Figure 9. The SEM cross-sectional image of ZnSe thin film deposited on glass substrate.

Figure 10(a) shows the refractive index as a function of wavelength. The dispersion of refractive index follows the Cauchy dispersion relation with two fitting parameters: a = 2.49 and b = 93714.88 given by equation below [38,39]:

$$n(\lambda) = a + \frac{b}{\lambda^2} \tag{37}$$

Since the refractive index data fitted well with Cauchy dispersion relation, it is possible to estimate refractive index data in wide wavelength region.

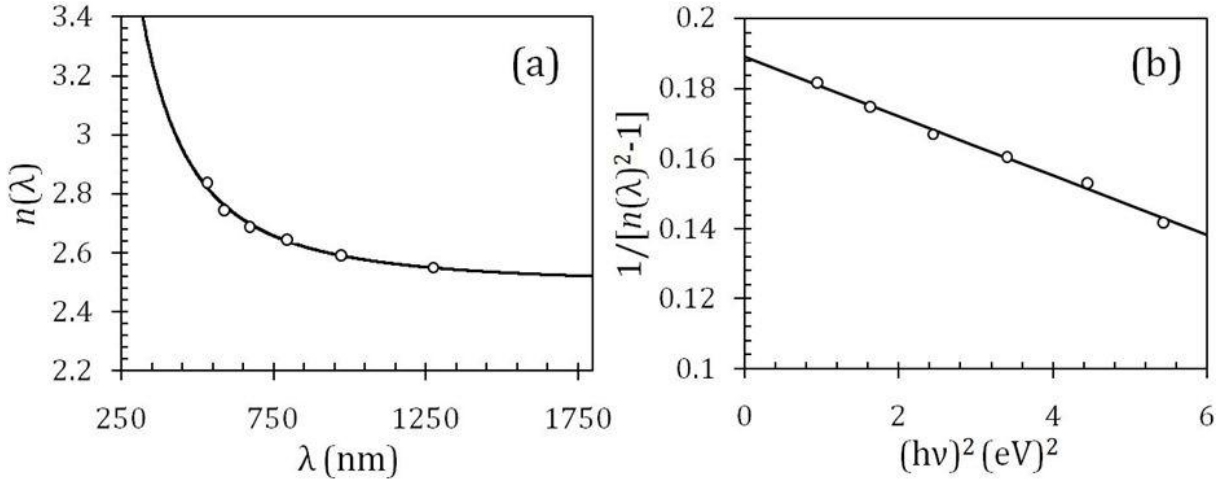

Figure 10. (a) Empty circles correspond to refractive index estimated from SWEM; solid line corresponds to Cauchy dispersion relation, (b) empty circles correspond to refractive index estimated from SWEM; solid line corresponds to WDD single oscillator model.

Although the Cauchy dispersion relation successfully represents the experimental dispersion of refractive index data, it does not give much physical information. Therefore, Wemple-DeDomenico (WDD) single oscillator model has been adopted to explain the dispersion of the refractive index [35,36]. It can be approximated that inter-band transitions are contributed by individual oscillator and each valence band electron is an oscillator. Generally, in the transparent region the real part of the dielectric constant can be expressed as a summation of all possible inter-band oscillator strength in the Brillouin zone of crystalline materials. Wemple and DeDomenico suggested that if one such oscillator's strength is stronger than the summation of that of the other oscillators, then below the band gap (in the transparent region) the real part of refractive index can be expressed as [40]:

$$\varepsilon_1 - 1 = n(\lambda)^2 - 1 = \frac{E_d E_o}{\left[E_o^2 - (h\nu)^2\right]} \tag{38}$$

where, E_d, E_o and hν are the dispersion energy, oscillator energy and incident photon energy respectively. Figure 10(b) shows refractive index data as a function of the incident photon energy, where the refractive index data has been plotted in $[n(\lambda)^2 - 1]^{-1}$ form. The first equality sign appeared in equation (38) originated from the fact that in the low energy region below the absorption

edge with negligible absorption, the real part of the dielectric constant can be expressed as: $\varepsilon_1 = n(\lambda)^2 - k(\lambda)^2 \sim n(\lambda)^2$. Figure 10(b) shows a least square fitted straight line with a correlation coefficient R^2 = 0.998. The slope (m) of the fitted line is equal to the reciprocal of the product of E_d and E_o and the Y-intercept (C) corresponds to E_o/E_d. Using the slope and the intercept, the dispersion and the oscillator energies have been estimated using equations; $E_d = \sqrt{m/C}$ and $E_o = \sqrt{m \cdot C}$ respectively. The oscillator energy is related to the band gap and the dispersion energy is related to the dielectric loss. Most importantly, E_d and E_o can be related to the moments of the optical spectra given by the following relations [41]:

$$E_o^2 = \frac{M_2}{M_3};\ E_d^2 = \frac{M_2^3}{M_3} \tag{39}$$

Equation (39) relates the real and imaginary parts of the dielectric constants. M_2 and M_3 are the 2nd and 3rd moments of the optical spectra $\varepsilon_2(E)$ given by equation; $M_r = \int_{E_g}^{\infty} E^{3-2r}\varepsilon_2(E)dE$, where $\varepsilon_2(E)$ is also the representative of the imaginary part of dielectric constant [21]. On the other hand, E_d, E_o along with the real part of the dielectric constant $\varepsilon_1(E)$ can be estimated from $n(\lambda)$ data below the optical absorption edge using equation (38). However, a relation between $\varepsilon_1(E)$ and $\varepsilon_2(E)$ can also be established directly from Kramers-Kronig relation which is beyond the scope of this paper. However, the values of M_2 and M_2 can be determined simply by rearranging equation (39) as: $M_2 = E_d/E_o$ and $M_3 = E_d/E_o^3$.

E_o, E_d, M_2, M_3 for our ZnSe thin film are given in Table 4. M_2 is a measure of spectral width of the absorption spectra which is estimated as 5.28 and it is found to be smaller than the previously reported data [6]. It means that the variance around the optical band gap is smaller in our case. This could be attributed to the better crystallinity and good surface morphology associated with the reduced defect states in the forbidden zone. This assumption is further supported by smaller dispersion energy of 24.95 e*V* obtained in the present study, compared to that of 30.88 e*V* obtained in the previous study for ZnSe thin film under extreme laser annealing condition [6]. Since dispersion energy E_d increases with dielectric loss, the lower the E_d the better the crystallinity in terms of surface morphology and defect-states.

The E_d value obtained from WDD model has been used to estimate the inter-atomic bond characteristic using the following equation [27]:

$$E_d = \beta_o N_C Z_a N_e \text{ (eV)} \tag{40}$$

Here, N_e is the number of effective valence electrons per anion, N_C is the number of the nearest neighbouring anion for a cation, which is 4 for ZnSe since each Zn ion is situated in a tetrahedral site formed by Se ion (see inset of Figure 1(b)) and Z_a = 2 is the chemical valency of Se anion.

Therefore, N_e can be calculated using the following relation:

$$N_e = \frac{A_{Se} \times V_{Se} + A_{Zn} \times V_{Zn}}{A_{Se}} \tag{41}$$

Here, A_{Se} and A_{Zn} are atom% of Se and Zn respectively in the ZnSe; A_{Se} and A_{Zn} are 59.85 and 41.15 respectively experimentally obtained from SEM-EDX analysis; $V_{Se} = 6$ and $V_{Zn} = 2$ are the

valence electron numbers of Se and Zn respectively. Thus, following equation (40), β_o has been evaluated as 0.42, suggesting the nature of the chemical bonds in ZnSe to be covalent. Our β_o value also shows excellent agreement with the classic paper of Wemple et al. [25], where the β_o has been calculated for the bulk material. However, our result shows larger value for $\beta_o$than recently reported result for ZnSe thin film [6]. This could possibly be attributed to a better bond ordering in the present sample due to the high temperature deposition and post deposition annealing. From the WDD relation it is possible to estimate the static dielectric constant in very long wavelength region by replacing $h\nu \to 0$ (which is equivalent to $\lambda \to \infty$) in equation (38):

$$n(\infty) = \sqrt{1 + \frac{E_d}{E_o}} \tag{42}$$

where, $\varepsilon_{\propto 1} = n(\infty)^2$ is the Static dielectric constant and it takes account of electronic, ionic and space charge polarizations altogether. The experimental refractive data can also be used to estimate the carrier concentration to effective mass ratio using the following equation [39,42]:

$$n(\lambda)^2 = \varepsilon_{\propto 2} - \left(\frac{e^2}{\pi c^2 \epsilon_0}\right)\left(\frac{N}{m^*}\right)\lambda^2 \tag{43}$$

Figure 11(a) shows $n(\lambda)^2$ as function of λ^2. Strong dispersive behaviour can be observed in high energy (short wavelength) region. At energy larger than the band gap, the incident photon is completely absorbed and thereby the electromagnetic wave cannot propagate through the thin film. In the low energy (long wavelength) region, normal dispersion is observed and the extrapolation of the low energy slope to $\lambda^2 = 0$ provides $\varepsilon_{\propto 2}$ which corresponds to the electronic dielectric constant at high frequency region since, only electrons can respond to the high energy photon through inter band optical transition. The values of $\varepsilon_{\propto 1}$ and $\varepsilon_{\propto 2}$ are listed in Table 4.

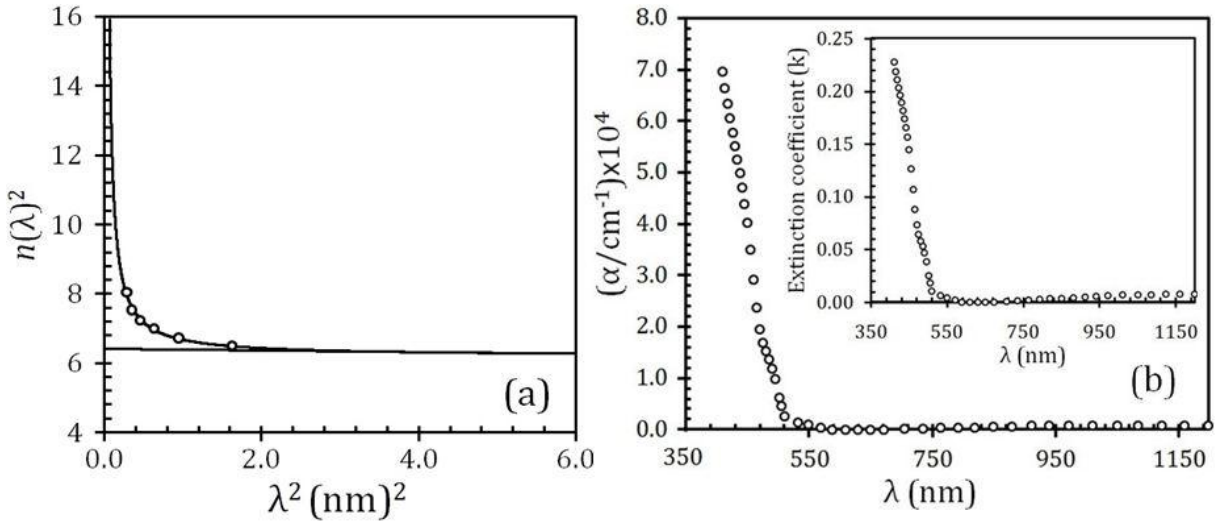

Figure 11. (a) Dispersion of dielectric constant, (b) Absorption coefficient α as a function of incident photon wavelength λ and the inset shows the corresponding extinction coefficient spectrum.

Table 4. Electro-optical parameters for ZnSe thin film.

Electro optical parameter	value
Optical Energy gap, E_g (e*V*)	2.64
Oscillator Energy, E_o (e*V*)	4.72
Dispersion Energy, E_d (e*V*)	24.95
The energy Ratio, $E_o/2E_g$	0.90
The momentum, M_2	5.28
The momentum, M_3	0.23
The static Refractive Index, $n(\infty)$	2.53
The dielectric constant, $\varepsilon_{\propto 1}$	6.28
The dielectric constant, $\varepsilon_{\propto 2}$	6.41

From the transmittance data, absorption coefficient and extinction coefficient have been calculated. Absorbance is related to absorption coefficient (α) by following relation [42]:

$$\alpha = \frac{1}{d}\ln(A) \tag{44}$$

Here, *A* is the absorbance and *d* is the thickness of the thin film. Absorbance can be calculated from the T_α envelope obtained from the experimental transmittance data (Figure 8(b)), using the following equations [38]:

$$A = \frac{B+\left[B^2+2qT_\alpha(1-R_2R_3)\right]^{\frac{1}{2}}}{q} \tag{45}$$

$$B = (R_1-1)(R_2-1)(R_3-1); \tag{46}$$

$$q = 2T_\alpha(R_1R_2 - R_1R_3 - R_1R_2R_3) \tag{47}$$

where, R_1, R_2 and R_3 are the reflectance values of the air-film, film-substrate and substrate-air interfaces respectively and are given by following equations:

$$R_1 = \left[\frac{1-n(\lambda)}{1+n(\lambda)}\right]^2;\ R_2 = \left[\frac{n(\lambda)-S(\lambda)}{n(\lambda)+S(\lambda)}\right]^2;\ R_3 = \left[\frac{S(\lambda)-1}{S(\lambda)+1}\right]^2 \tag{48}$$

Here, $n(\lambda)$ and $S(\lambda)$ are the refractive indexes of the thin film and the glass substrate respectively. Figure 11(b) shows the absorption coefficient as function of wavelength calculated using equations (44–48).

From Figure 11(b), the absorption edge can be found to occur around 510 nm. This wavelength is slightly smaller than the previously reported value for ZnSe thin film [6]. This discrepancy could be an indication of better crystallinity associated with more uniform and possibly coherent crystallites in case of the present sample when compared to the previous report. However, in order to establish such argument on a solid ground it is rather imperative to conduct optical and structural study on a series of thin film samples having different thermal histories prepared under same

experimental setup, which is underway. The absorption coefficient is directly proportional to the extinction coefficient (k) by following relation:

$$k = \frac{\alpha\lambda}{4\pi} \tag{49}$$

The inset of Figure 11(b) shows the extinction coefficient as function wavelength. Extinction coefficient has significant practical importance since it represents the loss of electromagnetic wave inside the thin film of interest. From Figure 11(b) it is clear that this thin film can function as a good optical material at relatively low wavelengths (down to 510 nm) of the visible spectrum.

Another important parameter to characterize a semiconductor is its band gap (E_g) which has been estimated from the energy dependent absorption coefficient data at the absorption edge using the Tauc's relation [43] as follows:

$$\alpha h\nu = \alpha_o(h\nu - E_g)^m \tag{50}$$

Here, α is the absorption coefficient, E_g is the band gap, α_o is the band tailing parameter and m is the power factor of the transition mode which depends on crystal structure of the materials and the type of electronic transition that leads to formation of absorption edge in the optical transmission spectrum. The values of m for indirect allowed, direct allowed, indirect forbidden and direct forbidden transitions are 2, 0.5, 1.5 and 3 respectively. Now equation (50) can be slightly rearranged as: $\ln(\alpha h\nu) = \ln\alpha_o + m \cdot \ln(h\nu - E_g)$. Hence, the slope of the plot $\ln(\alpha h\nu)$ vs. $\ln(h\nu - E_g)$ around the absorption edge gives the value of m which has been found to be $m = 0.508 \approx 0.5$ from the linearly fitted line-equation shown in the inset-plot of Figure 12(a). Therefore, the Tauc's relation can safely be written for the present sample as:

$$(\alpha h\nu)^2 = \alpha_o(h\nu - E_g) \tag{51}$$

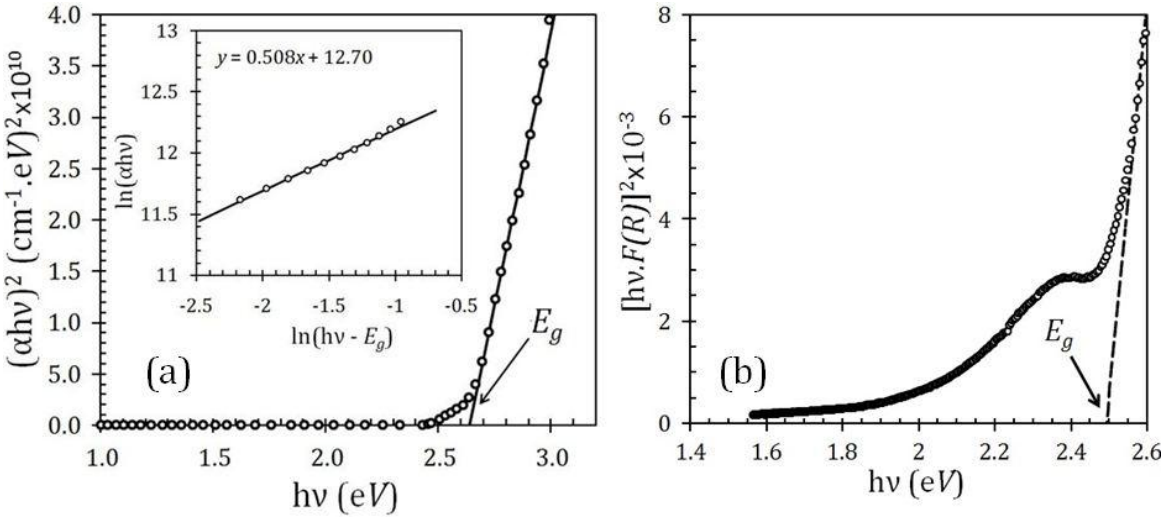

Figure 12. (a) The Tauc's plot for the determination optical band gap. The inset shows $\ln(\alpha h\nu)$ vs. $\ln(h\nu - E_g)$ plot along with the equation for linear fit, (b) The Tauc's plot for the determination optical band gap of powder using the Kubelka-Munk function.

Figure 12(a) shows the plot of $(\alpha h\nu)^2$ as a function of photon energy $h\nu$ also known as the Tauc's plot. From the plot, optical band gap can now be determined firstly by fitting a straight line around the absorption edge of the plot and then by estimating the point of intersection of the fitted line with the $h\nu$-axis at $(\alpha h\nu)^2 = 0$. The band gap obtained from the Tauc's plot has been found to be 2.64 eV which appears to be a quite reasonable value when compared with previously reported results [2,6,12,13,16,20,23].

Moreover, it is rather interesting to compare the band gap required for optical absorption of the deposited film with that of the pulverized source powder. In order to determine the band gap of opaque powder material for direct transition, it is a common practice to use the Tauc's relation given by equation (51) provided that the absorption coefficient is now given by the following equation [44]:

$$\alpha = \tau_o F(R)/(2v_p) \tag{52}$$

where, τ_o is the scattering coefficient, v_p is the volume fraction of the absorbing species and $F(R)$ is the Kubelka-Munk function given by:

$$F(R) = (1-R)^2/(2R) \tag{53}$$

where, R is the measured diffuse reflectance of powder sample. Now, neglecting the dependence of τ_o and v_p on incident wavelength, the absorption coefficient can be written as;

$$\alpha = \{\tau_o/(2v_p)\} \cdot F(R) = A \cdot F(R) \tag{54}$$

Here, A is a constant. Therefore, combining equation (51) and (54), we get:

$$[h\nu \cdot F(R)]^2 = \alpha_o^{/}(h\nu - E_g) \tag{55}$$

where, $\alpha_o^{/}$ is a constant. According to equation (55), at the absorption edge, $[h\nu \cdot F(R)]^2$ should vary linearly with $(h\nu)$ and the optical band gap could be obtained by linearly extrapolating the most steep, linear portion of $[h\nu \cdot F(R)]^2$ vs. $(h\nu)$ plot to $[h\nu \cdot F(R)]^2 = 0$ where, $h\nu = E_g$. Figure 12(b) depicts such a plot for our ZnSe source powder, where the diffuse reflectance data were taken within a wavelength range of 200–600 nm at 1 nm interval. From the extrapolation represented by the dotted line, it can be found that our powdered ZnSe source has an optical band gap of 2.5 eV for direct transition. This indicates an obvious blue shift in the electronic transition energy of the deposited ZnSe thin film by 0.14 eV when compared to that of the source powder. Similar behaviour was reported for thermally evaporated ZnSe thin films from bulk ZnSe [6], which could be qualitatively comprehended in terms of 3D quantum confinement effect associated with crystal/particle size reduction to nano or below nano-scale as a first approximation. The basic 3D quantum confinement model is actually based on effective mass approximation relation for quantum dots given by:

$$\Delta E_g = E_g^{nano} - E_g^{bulk} = \{h^2/(2m_o D^2)\} \cdot (1/m_e^* + 1/m_h^*) - \{(3.6e^2)/(4\pi\epsilon_r\epsilon_o D)\} \tag{56}$$

where, ΔE_g is the blue shift in band gap energy; h, e, m_o, m_e^*, m_h^*, ϵ_r, ϵ_o and D are the Plank's constant, electron charge, electron rest mass, effective mass of electron, effective mass of hole, relative permittivity of the medium, vacuum permittivity and particle/crystallite size respectively. The above equation clearly entails for a blue shift in band gap with a decrement in crystallite size. Having said that, a careful comparison between Figure 1(a) and 1(b) reveals that the actual film is subjected to a significant peak broadening in relation to that of the source powder. As a matter of fact, the instrumental broadening is around 80% of the observed peak width in case of our source powder indicating only a minute size broadening effect. Hence, the crystal size of the source ZnSe obtained from the standard Debye-Scherrer model comes out to be 321 nm, which is way beyond the maximum reliable size-limit (100 nm) that can be calculated from the model itself, suggesting that the average particle/crystallite size of the source powder has to be above 100 nm. Henceforth, we could safely infer that the reduction in particle/crystallite size from above 100 nm to a range of 2–26 nm after the film deposition is the most conceivable catalyst at hand to induce the observed blue shift in band gap in our case.

Additionally, it has been shown by K. Tanaka [45] that there exits an approximate relation between the band gap and oscillator energy given by the form: $E_o/2E_g \sim 1$. For our sample this ratio has been calculated to be 0.9 which is approximately equal to 1. Although this ratio has been reported to fall within an excellent range of 1–1.04 for pulsed laser annealed ZnSe thin films [6] the standard WDD model analysis by Gullu et al. [23] indicated this ratio to vary from 0.5 to 0.6 for TVD ZnSe thin film annealed at 300 ℃ to 500 ℃. From a more contemporary study on TVD ZnSe thin film without any post-deposition annealing treatment [12], this energy ratio can be calculated to be around 0.7. In view of the above findings, we can only state that for our vacuum annealed TVD thin film sample, the energy ratio appears to be close to 1. However, the observed deviation from unity might be associated with some structural and morphological disorders, which could lead to a distribution of oscillator energies instead of a single-valued one as originally proposed by the ideal WDD model.

It is evident from the detailed structural and optical study that our thermal vapour deposited ZnSe thin film is structurally sound regardless the quality of the substrate used. All the structural and optical parameters appear to be rather reasonable and even sometimes better. The low optical dispersion energy and optical moment as well as the observed β_o value indicate high degree of crystallinity. This observation is further supported by the combined SEM and XRD analysis which indicate the possible absence of interfaces within the particles formed from defect ordering.

4. Conclusion

ZnSe thin film was prepared on a readily available soda-lime glass substrate by thermal evaporation technique. Detailed structural characterization of ZnSe thin film using XRD was reported. X-ray diffraction data confirmed the polycrystalline nature of the film with (111), (220) and (311) peaks having zincblende structure. Texture analysis of ZnSe thin film was performed by pole-figure measurement. (111) plane showed strong orientation around 15 ° and 60 ° with substrate normal and also explained some anomalous variations observed in the relative intensity ratios of the diffraction peaks of the thin film. Crystallite size was estimated from the width of the diffraction peaks using Debye-Scherrer, Size-Strain plot, Williamson-Hall, modified Williamson-Hall model and the so called approximation model based on the separate contribution from the size and strain

broadening. The crystallite size was found to fall within a narrow range of 12–17 nm depending on the model used which exhibited good agreement with the particle size range of 10–18 nm obtained from SEM image analysis. This is an indication that most of the observed particles are crystallographically coherent. The change of lattice volume in thin film is attributed to local lattice strain. The deviation of average internal strain obtained from W-H method by ~10^{-3} from that of the local lattice strain obtained from Nelson-Riley relation is believed to be associated with thin film strain relaxation through micro-crack formation. The other mechanical and thermodynamic parameters such as stress, dislocation density and anisotropic energy density were reported. The film thickness estimated using Swanepoel's envelope method was ~374.9 nm which exhibited good agreement with the thickness obtained from SEM image within the experimental standard deviation. Refractive index data exhibited strong dispersive behaviour in the short wavelength region, suggesting optical absorption in the short wavelength range. The most important parameter optical band gap was estimated to be 2.64 e*V*. WDD single oscillator model was used to estimate dispersion energy and Oscillator energy from the low energy refractive index data. Low dispersion energy and smaller optical moments suggest that better crystallinity has been obtained in the present sample which is also supported by the observed crystallographic coherency of individual particles obtained from crystal-size measurement data. The observed blue-shift in optical transition energy of the thin film by 0.14 e*V* with respect to that of the source powder was attributed to quantum size effect.

Conflict of Interest

The authors declare that there is no conflict of interest in this paper.

Reference

1. Mehta C, Saini GSS, Abbas JM, et al. (2009) Effect of deposition parameters on structural, optical and electrical properties of nanocrystalline ZnSe thin films. *Appl Surf Sci* 256: 608–614.
2. Venkatachalam S, Jeyachandran YL, Sureshkumar P, et al. (2007) Characterization of vacuum-evaporated ZnSe thin films. *Mater Charact* 58: 794–799.
3. Xia M, Liu C, Zhao Z, et al. (2015) Formation and optical properties of ZnSe and ZnS nanocrystals in glasses. *J Non-Cryst Solids* 429: 79–82.
4. Kalita PKR, Sarma BK, Das HL (2000) Structural characterization of vacuum evaporated ZnSe thin films. *B Mater Sci* 23: 313–317.
5. Subbaiah YPV, Prathap P, Devika M, et al. (2005) Close-spaced evaporated ZnSe films: Preparation and characterization. *Physica B* 365: 240–246.
6. Hassanien AS, Aly KA, Akl AA (2016) Study of optical properties of thermally evaporated ZnSe thin films annealed at different pulsed laser powers. *J Alloy Compd* 685: 733–742.
7. Lokhande CD, Patil PS, Tributsch H, et al. (1998) ZnSe thin films by chemical bath deposition method. *Sol Energ Mat Sol C* 55: 379–393.
8. Sagadevan S, Das I (2016) Chemical bath deposition (CBD) of zinc selenide (ZnSe) thin films and characterisation. *Aust J Mech Eng* 1–6.
9. Patidar D, Rathore KS, Saxena NS, et al. (2008) Determination of optical and electrical properties of ZnSe thin films. *J Mod Optic* 55: 3041–3047.

10. Mittal V, Sessions NP, Wilkinson JS, et al. (2017) Optical quality ZnSe films and low loss wave guides on Si substrates for mid-infrared. *Opt Mater Express* 7: 712–725.
11. Ismail ME, Shaaban ER, Hagary ME (2016) A new method for calculating the refractive index of semiconductor thin films retrieved from their transmission spectra. *J Alloy Compd* 663: 20–29.
12. Desai HN, Dhimmar JM, Modi BP (2016) Optical and dispersion analysis of Zinc Selenide thin film. *Mater Today Proc* 3: 1650–1657.
13. Khan NA, Saleem A, Satti AR, et al. (2016) Post deposition annealing: a route to band gap tailoring of ZnSe thin films. *J Mater Sci-Mater El* 27: 9755–9760.
14. Yuvaraj D, Kumar RR, Selvan VT, et al. (2014) Growth of ZnSe nano and microstructures at high vacuum by thermal evaporation. *Appl Nanosci* 4: 469–475.
15. Lohar GM, Shinde SK, Fulari VJ (2014) Structural, morphological, optical and photoluminescent properties of spray-deposited ZnSe thin film. *J Semiconduct* 35: 113001.
16. Zhang X, Wang D, Beres M, et al. (2013) Zincblende-wurtzite phase transformation of ZnSe films by pulsed laser deposition with nitrogen doping. *Appl Phys Lett* 103: 082111.
17. Khanand TM, BiBi T (2012) Compatibility and optoelectronic of ZnSe nano crystalline thin film. *Chinese Phys B* 21: 3097303.
18. Aqili A, Ali Z, Hussain Z (2012) Optical and structural properties of silver doped ZnSe thin films prepared by CSS and ion exchange process. *Thin Film Solar Technology IV, Proc. Of SPIE* 8470: 84700H.
19. Khairnar U, Behere S, Pawar P (2012) Optical properties of polycrystalline Zinc Selenide thin films. *Mater Sci Appl* 3: 36–40.
20. Ashraf M, Akhtar SMJ, Khan AF, et al. (2011) Effect of annealing on structural and optoelectronic properties of nanostructured ZnSe thin films. *J Alloy Compd* 509: 2414–2419.
21. Ismail ME, Hagary ME, Shaab ER, et al. (2012) Microstructure and optical studies of electron beam evaporated $ZnSe_{1-x}Te_x$ nanocrystalline thin films. *J Alloy Compd* 532: 16–24.
22. Ahamed MGSB, Nagarethinam VS, Balu AR, et al. (2010) Influence of substrate temperature on the properties of electron beam evaporated ZnSe films. *Cryst Res Technol* 45: 421–426.
23. Güllü HH, Coşkun E, Parlak M (2015) Investigation of optical parameters of thermally evaporated ZnSe thin films. *Phys Status Solidi C* 12: 1224–1228.
24. Kalita A, Kalita MPC (2017) Williamson-Hall analysis and optical properties of small sized ZnO nanocrystals. *Physica E* 92: 36–40.
25. Kumar BR, Hymavathi B (2017) X-ray peak profile analysis of solid-state sintered alumina doped zinc oxide ceramics by Williamson-Hall and size-strain plot methods. *J Asian Ceram Soc* 5: 94–103.
26. Prabhu YT, Rao KV, Kumar VSS, et al. (2014) X-Ray analysis by Williamson-Hall and size-strain slot methods of ZnO Nanoparticles with fuel variation. *World J Nano Sci Eng* 4: 21–28.
27. Garg P, Rai R, Singh BK, et al. (2014) Structural characterization of "as-deposited" cesium iodide films studied by X-ray diffraction and transmission electron microscopy techniques. *Nucl Instrum Meth A* 736: 128–134.
28. Monshi A, Foroughi MR, Monshi MR (2012) Modified Scherrer equation to estimate more accurately nano-crystallite size using XRD. *World J Nano Sci Eng* 2: 154–160.
29. Sivasankaran S, Sivaprasad K, Narayanasamy R, et al. (2011) X-ray peak broadening analysis of AA 6061_{100-x}–x wt.% Al_2O_3 nanocomposite prepared by mechanical alloying. *Mater Charact* 62: 661–672.

30. Zak AK, Aulmajid WH (2011) X-ray analysis of ZnO nanoparticles by Williamson-Hall and Size strain plot method. *Solid State Sci* 13: 251–256.
31. Bushroa AR, Rahbari RG, Masjuki HH, et al. (2012) Approximation of crystallite size and the microstrain via XRD line broadening analysis in TiSiN thin films. *Vacuum* 86: 1107–1112.
32. Ou K, Wang S, Wan G, et al. (2017) Structural, morphological and optical properties of ZnO films by thermal oxidation of ZnSe films. *Thin Solid Films* 634: 51–55.
33. Nelson JB, Riley PD (1945) An experimental investigation of extrapolation methods in the derivation of accurate unit-cell dimensions of crystals. *Proc Phys Soc* 57: 160–177.
34. Kim MJ, Lee SH, Kim HT, et al. (2013) Physical properties of ZnSe thin films depending on the process parameters. *Mol Cryst Liq Cryst* 586: 129–137.
35. Morales M, Chateigner D, Lutterotti L (2009) X-ray textural and microstructural characterizations by using the combined analysis approach for the optical optimisation of micro- and nano-structured thin films. *Thin Solid Films* 517: 6264–6270.
36. Rizzoa A, Taglientea MA, Caneveb L, et al. (2000) The influence of the momentum transfer on the structural and optical properties of ZnSe thin films prepared by r.f. magnetron sputtering. *Thin Solid Films* 368: 8–14.
37. Swanepoel R (1983) Determination of the thickness and optical constants of amorphous silicon. *J Phys E Sci Instrum* 16: 1214–1222.
38. Dahshan A, Amer HH, Aly KA (2008) Compositional dependence of the optical constants of amorphous $Ge_xAs_{20}Se_{80-x}$ thin films. *J Phys D Appl Phys* 41: 215401.
39. Aly KA (2010) Optical band gap and refractive index dispersion parameters of $As_xSe_{70}Te_{30-x}$ ($0 \leq x \leq 30$ at.%) amorphous films. *Appl Phys A-Mater* 99: 913–919.
40. Wemple SH, DeDomenico M (1971) Behaviour of electronic dielectric constant in covalent and ionic materials. *Phys Rev B* 3: 1338–1351.
41. Wemple SH, DiDomenico M (1969) Optical dispersion and the structure of solids. *Phys Rev Lett* 23: 1156–1160.
42. Connell GAN, Lewis AJ (1973) Comments on the evidence for sharp and gradual optical absorption edges in amorphous germanium. *Phys Status Solidi B* 60: 291–298.
43. Tauc J (1974) *Amorphous and Liquid Semiconductors*, New York: Plenum Publishing Corporation.
44. Venugopal B, Nandan B, Ayyachamy A, et al. (2014) Influence of manganese ions in the band gap of tin oxide nanoparticles: structure, microstructure and optical studies. *RSC Adv* 4: 6141–6150.
45. Tanaka K (1980) Optical properties and photoinduced changes in amorphous AsS films. *Thin Solid Films* 66: 271–279.